Journal of Nuclear Materials 556 (2021) 153172

Contents lists available at ScienceDirect

Journal of Nuclear Materials

journal homepage: www.elsevier.com/locate/jnucmat

Synthesis and thermodynamics of uranium-incorporated α-Fe_2O_3 nanoparticles

Andy Lam[a,b], Forrest Hyler[c], Olwen Stagg[d], Katherine Morris[d], Samuel Shaw[d,*], Jesús M. Velázquez[c,*], Alexandra Navrotsky[a,b,c,e,*]

[a] Peter A. Rock Thermochemistry Laboratory, University of California Davis, Davis, CA 95616, United States
[b] Department of Materials Science and Engineering, University of California Davis, Davis, CA 95616, United States
[c] Department of Chemistry, University of California Davis, Davis, CA 95616, United States
[d] Research Centre for Radwaste Disposal and Williamson Research Centre for Molecular Environmental Science, School of Earth, Atmospheric and Environmental Sciences, The University of Manchester, Manchester, M13 9PL, United Kingdom
[e] School of Molecular Sciences and Navrotsky Eyring Center for Materials of the Universe, Arizona State University, Tempe, AZ 85287, United States

ARTICLE INFO

Article history:
Received 28 April 2021
Revised 25 June 2021
Accepted 3 July 2021
Available online 7 July 2021

Keywords:
Uranyl
Iron oxides
Hematite
Water remediation
Calorimetry
X-ray absorption spectroscopy

ABSTRACT

Hematite nanoparticles were synthesized with U(VI) in circumneutral water through a coprecipitation and hydrothermal treatment process. XRD, TEM, and EXAFS analyses reveal that uranium may aggregate along grain boundaries and occupy Fe sites within hematite. The described synthesis method produces crystalline, single-phase iron oxide nanoparticles absent of surface-bound uranyl complexes. EXAFS data were comparable to spectra from existing studies whose syntheses were more representative of naturally occurring, extended aging processes. This work provides and validates an accelerated method of synthesizing uranium-immobilized iron oxide nanoparticles for further mechanistic studies. High temperature oxide melt solution calorimetry measurements were performed to calculate the thermodynamic stability of uranium-incorporated iron oxide nanoparticles. Increasing uranium content within hematite resulted in more positive formation enthalpies. Standard formation enthalpies of $U_xFe_{2-2x}O_3$ were as high as 76.88 ± 2.83 kJ/mol relative to their binary oxides, or -764.04 ± 3.74 kJ/mol relative to their constituent elements, at x = 0.037. Data on the thermodynamic stability of uranium retention pathways may assist in predicting waste uranyl remobilization, as well as in developing more effective methods to retain uranium captured from aqueous environments.

1. Introduction

Uranium (U), in the form of uranyl ions (UO_2^{2+}), can be present as a radiological contaminant in surface and subsurface environmental systems (e.g., groundwater). Potential sources of contamination include coal power plant emissions, leachate from uranium ore mining, and degraded radioactive waste from both military and civilian sources, all of which could pose contamination risks to local ecology and water sources for human consumption [1]. Exposure to this persistent, mobile toxin has been found to induce long-lasting detrimental effects to humans [2,3]. Legacy radioactive waste storage facilities at sites across the world, e.g., the U.S. DOE Hanford site, have exceeded their planned life expectancy and have been shown to leak into their surrounding environment [4,5]. An approach for legacy and modern high-level wastes (HLW) and Intermediate-level wastes (ILW) is solidification with inert species (e.g., vitrification) and storage within steel containers, where the radioactive elements will decay over timescales of hundreds of years to millennia [5,6]. Multiple layers of containment further protect this solidified waste from external perturbations, although self-induced and environmentally-driven corrosion and eventual leakage remain a challenge and a risk [5–8]. It is imperative that such waste remains unperturbed for millennia (e.g., within a geological storage facility), allowing the contained radioisotopes to decay.

Engineered materials, such as steel linings used to contain radioactive waste, may gradually corrode, and transform to environmentally ubiquitous and stable iron oxides (e.g., hematite and goethite). Depending on environmental conditions, a variety of iron oxide and oxyhydroxide polymorphs can form [9]. Hematite (α-Fe_2O_3) is stable in a wide range of environmental and geolog-

* Corresponding authors.
E-mail addresses: adlam@ucdavis.edu (A. Lam), fphyler@ucdavis.edu (F. Hyler), olwen.stagg@manchester.ac.uk (O. Stagg), katherine.morris@manchester.ac.uk (K. Morris), sam.shaw@manchester.ac.uk (S. Shaw), jevelazquez@ucdavis.edu (J.M. Velázquez), Alexandra.Navrotsky@asu.edu (A. Navrotsky).

https://doi.org/10.1016/j.jnucmat.2021.153172
0022-3115/

ical conditions. Hematite nanoparticles have been shown to be highly effective at adsorbing aqueous heavy metal and actinide ions, enabling their application to water remediation [10–13]. It has been well established that aqueous uranium may become immobilized by iron oxide polymorphs by a combination of adsorption on the surface and incorporation within the structure of these nanoparticles [14–16]. While surface adsorption may be effective in retarding aqueous uranium migration in the subsurface, changes in biogeochemical conditions (e.g., pH) or presence of competing species may remobilize uranium [17]. Kinetic and structural studies have demonstrated additional pathways where uranium is more strongly retained within the crystal structure of α-Fe_2O_3 [10,16,18–20]. Understanding this behavior is paramount to understand the role and significance of iron oxides immobilizing radionuclides in future geological disposal facilities for radioactive waste, as well as the efficacy of iron oxides as a long-term capture and storage medium for uranium from contaminated effluents.

The ability of α-Fe_2O_3 to structurally incorporate uranium, rather than only surface adsorb it, provides a promising secondary uranium immobilization pathway. The coordination environment of the more strongly restrained uranium has been studied for a variety of iron oxide polymorphs prevalent in differing environmental conditions. Research has generally shown hematite to incorporate U within its Fe(III) sites during its formation from ferrihydrite, where U is present in uranyl coordination (i.e. distorted U-O octahedra) [16,19–21]. However, it is not yet understood how stability (thermodynamic and/or kinetic) scales with incorporation capacity within this phase. Conflicting interpretations propose different charge compensation schemes and point to different proposed local Fe vacancy configurations. The differences in potential energy of each configuration have been calculated, but experimental findings have not necessarily agreed with the lowest energy configurations. For example, a *trans*-corner Fe vacancy configuration surrounding U sites has been proposed, despite having a 112 kJ/mol energy penalty relative to single face-sharing and dual edge-sharing vacancy configurations [20]. These localized energy calculations do not necessarily represent the energetics of the bulk oxide, and the formation enthalpy of U-incorporated iron oxides is not yet known. Collecting such measurements will reveal the thermodynamic consequences of incorporation as a function of U content within the solid. With this information the ability of hematite to retain the captured actinide under geological time scales relevant to radioactive waste storage could be investigated.

Our key objective is to explore the effects of uranium incorporation on the thermodynamic stability of hematite. We describe herein the hydrothermal synthesis of hematite nanoparticles from precursor Fe(III) and U(VI) salts, defined as α-$U_xFe_{2-2x}O_3$. Extended X-ray absorption fine structure (EXAFS) was performed to explore local U coordination to validate structural incorporation and describe local U coordination. The effect of this structural incorporation on standard formation enthalpies of single-phase samples was measured using high temperature oxide melt solution calorimetry. Determining their formation enthalpies relative to mixtures of iron and uranium oxides may constrain stability of uranium retention over geologic timescales. These complementary techniques provide insight to the stability and effectiveness of iron oxides for radionuclide immobilization. These results provide new perspectives on the effectiveness of iron oxides to sequester uranium under both environmental and engineered conditions.

2. Experimental methods

2.1. Synthesis

Synthesis of uranium-incorporated hematite (α-$U_xFe_{2-2x}O_3$) has been achieved by mixing $Fe(NO_3)_3 \bullet 9H_2O$ (Sigma-Aldrich, ACS Reagent $\geq$ 98%) and $UO_2(NO_3)_2 \bullet 9H_2O$ (JT Baker, 'Baker Analyzed' Reagent) in 18.2 MΩ•cm deionized water. A total of 7 uranium-loaded samples were synthesized for calorimetric measurements. Uranyl concentrations ranged from 0.28 – 5.25 mM, while maintaining Fe(III) at 41 mM. 5 N NaOH (Fisher Scientific, Certified ACS) was used to titrate the acidic solution up to pH 7 ~ 9 while stirring at room temperature. Formation of colloidal ferrihydrite was observed around pH 5.6, at which point the precipitate was expected to favorably adsorb the uranyl species.

Hydrothermal treatment was used to accelerate the full transformation from ferrihydrite to hematite, preventing secondary phases (e.g., goethite, α-FeOOH) from otherwise forming [9]. 120 mL of the colloidal suspension was transferred to a 200 mL Teflon-lined hydrothermal vessel from Parr Instrument Co. The vessel was then sealed and placed into an oven at 180 °C for 24 to 72 h, followed by gradual cooling in air.

The product was collected at the bottom of the vessel and then shown to be fully transformed to hematite. Aliquots of the supernatant were preserved for elemental concentration analysis and were used to determine uranyl concentration in solution after synthesis. The precipitate was washed multiple times with DI water while agitating to remove residual salts, followed by centrifugation for at least 3 hat a relative centrifugal force (RFC) of roughly 800 x *g* between each step to collect the nanoparticles. The reaction for producing the final product is reported as Eq. (1):

$$x(UO_2)^{2+}_{(aq)} + (2-2x)Fe^{3+}_{(aq)} + (3-2x)H_2O_{(l)} \overset{180\ ^\circ C}{\rightarrow} U_xFe_{2-2x}O_{3\,(s)} + (6-4x)H^+_{(aq)} \quad (1)$$

This study focused on the stability of uranium well immobilized within hematite particles, absent of surface-bound uranyl and colloidal uranium-containing impurities. Additional washing steps using a solution of HCl below pH 2.5 were performed to achieve this, removing weakly retained uranium (e.g., surface adsorbed) [22,23]. Subsequent water washes were performed to clean and neutralize the product. Sample was then dispersed in ethanol and dried in air at 80 °C overnight.

2.2. Structural and electronic characterization

Identification of the desired iron oxide phase, and the absence of undesired secondary phases, is imperative for properly analyzing calorimetric data. Powder X-ray diffraction (PXRD) of the final product was performed to validate phase purity and crystallinity (Bruker D8 Advance, Cu K-α_1). Transmission electron microscopy (TEM) was performed to validate phase purity shown by XRD, as well assess uranium distribution within the iron oxide crystallites [19]. Imaging was performed using a JEOL 2100F at 200 kV and FEI Tecnai F30 at 300 kV, both in STEM mode. Samples were prepared by dispersing and sonicating powders in IPA and drop-casting onto carbon-backed Cu mesh grids. The grids were then baked out overnight at 80 °C and plasma-cleaned prior to imaging.

The coordination environments of uranium retained within hematite were determined by X-ray absorption spectroscopy (XAS). Uranium L_{III}-edge (17.1663 keV) spectra were collected on beamline B-18, Diamond Light Source (DLS) with the sample mounted in a liquid nitrogen cryostat and the data collected in fluorescence mode. Individual scans were calibrated with inline yttrium foil reference spectra, then merged to maximize the signal-to-noise ratio for the sample.

2.3. Stoichiometry determination

Thermogravimetric analysis (TGA) was performed in parallel with differential scanning calorimetry (DSC) using a Setaram Lab-

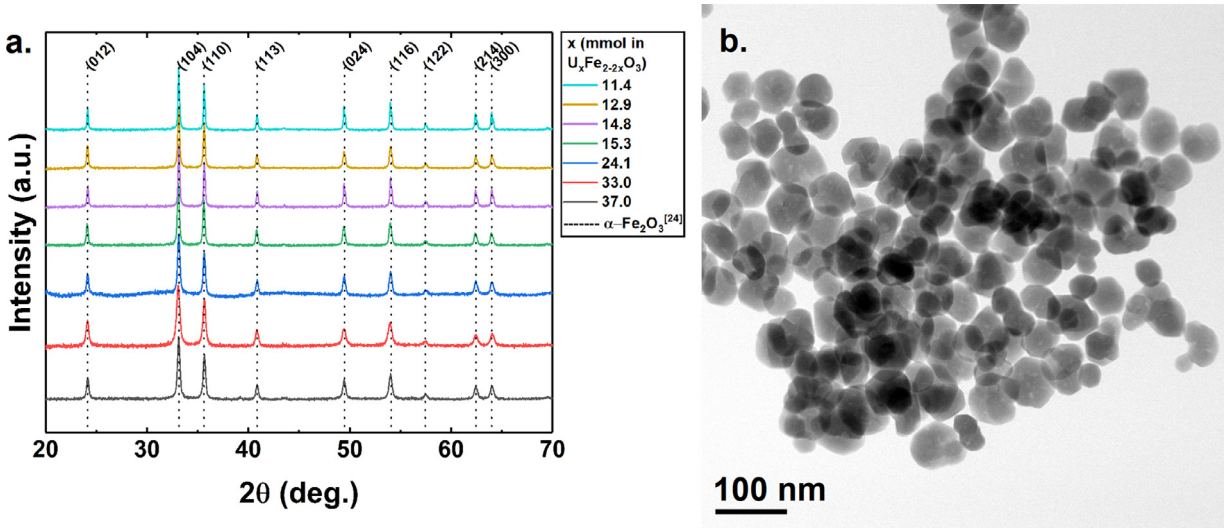

Fig. 1. XRD patterns acquired of single-phase hematite, coprecipitated with varying initial concentrations of uranyl ions (a) and representative bright field TEM micrograph of crystalline hematite nanoparticles (b).

sys Evo. Powders were pressed into pellets of 10–20 mg and placed in a 100 µL platinum crucible. Samples were heated from 25 to ≥ 800 °C at 10 °C/min while flushing the chamber with O_2. TGA quantified the amount of water adsorbed onto U-hematite particles. DSC data showed heat effects from dehydration and screened for other potential reactions induced by heating. A suitable drying temperature was selected based on these data. Uranium-free hematite analogues were then degassed under rough vacuum at 250 °C for 24 h. Surface areas of these analogues were determined using Brunauer-Emmett-Teller (BET) N_2 adsorption (Micromeritics Gemini VII 2390). Surface areas of U-free powders analogous to U-loaded samples averaged 15.05 ± 0.08 m^2/g, or 2403 ± 13 m^2/mol. Solid samples were digested in 5 N HCl at 90 °C then diluted to 2% HCl for inductively coupled plasma mass spectrometry (ICP-MS) analysis. Molar ratios of each element were then used to calculate the U/Fe stoichiometry of anhydrous product, defined as α-$U_xFe_{2-x}O_3$.

The differences in uranium content between the starting amount, amount remaining in solution after synthesis, and amount retained in the collected final product, were then used to calculate the amount of uranium lost to the successive washing and acid-leaching procedures. Lost uranium here is considered a combination of uranyl species adsorbed to hematite surfaces, poorly crystalline uranium-containing colloids, and general losses from repeated washing and centrifugation steps. At the same time, Fe concentrations confirmed that all the introduced Fe(III) had precipitated by the end of the reaction.

2.4. Calorimetry

High temperature oxide melt solution calorimetry was performed using a custom-built twin calvet calorimeter held at 700 °C with molten sodium molybdate ($3Na_2O{\bullet}4MoO_3$) as the solvent. Approximately ≤ 7 mg of sample was pelletized and dropped into the melt for each of multiple measurements. Oxygen gas was flushed above the solvent at 51.6 mL/min and bubbled through it at 5.9 mL/min. Flushing maintained a consistent atmosphere above the molten solvent, while bubbling through the solvent also stirred the melt and accelerated sample dissolution. The enthalpy of drops solution (ΔH_{ds}) was calculated by integrating the measured heat flow over time. This value was then used to calculate the standard formation enthalpy using appropriate thermochemical cycles. The calorimeter was calibrated against heat content of bulk α-Al_2O_3 powder.

3. Results

3.1. Synthesis and characterization of α-$U_xFe_{2-x}O_3$

XRD patterns reveal consistent production of crystalline hematite nanoparticles (Fig. 1). Each diffraction peak matched those of standard hematite[24], with peak broadening characteristic of nanoscale crystals. Furthermore, diffraction patterns suggest the absence of any uranium-bearing minerals in the acid-washed powders, possibly reflecting homogeneous UO_x distribution and low total U content. Whole-pattern Rietveld refinement (MDI Jade 6) of pristine powders suggested typical crystallite diameters of 25 – 95 nm (Figure A.5). Higher U content corresponded to lower crystallite size and elongation of the '*c*' cell parameter, whereas variations in the '*a*' parameter were minor (Figure A.5).

TEM corroborated findings by XRD that synthesized materials were single-phase crystalline nanoparticles, without any uranium-bearing colloids or secondary iron oxide phases (Fig. 2). The stark Z contrast of U relative to Fe and O in HAADF micrographs revealed that U is well distributed throughout individual nanocrystals, as well as along grain boundaries of aggregated nanoparticles (Fig. 2b, d). Uranium was not concentrated along particle rims, suggesting surface-bound uranium species were desorbed, and observable U had been resistant to acid washing. Evenly distributed U, as observed by EDS, further confirmed that uranium may homogenously persist throughout, in addition to clustering along the grain boundaries (Figure A.1, A.2). Results from subsequent characterization were then attributable to incorporated uranium and not complicated by external uranium-bearing species.

3.2. Uranium coordination and valence state

Considering the phase purity of synthesized samples, we attribute our U XAS spectra of $U_{0.033}Fe_{1.934}O_3$ to species retained within hematite, as opposed to any potential goethite or surface uranyl that may otherwise have been present. EXAFS fits of U L_{III}-edge spectra reveal that the axial oxygen bonds characteristic of uranyl are retained after hydrothermal induction into hematite, albeit with minor elongation relative to those referenced in liebigite [25]. This calculated uranyl-like bond length of 1.79 Å matches

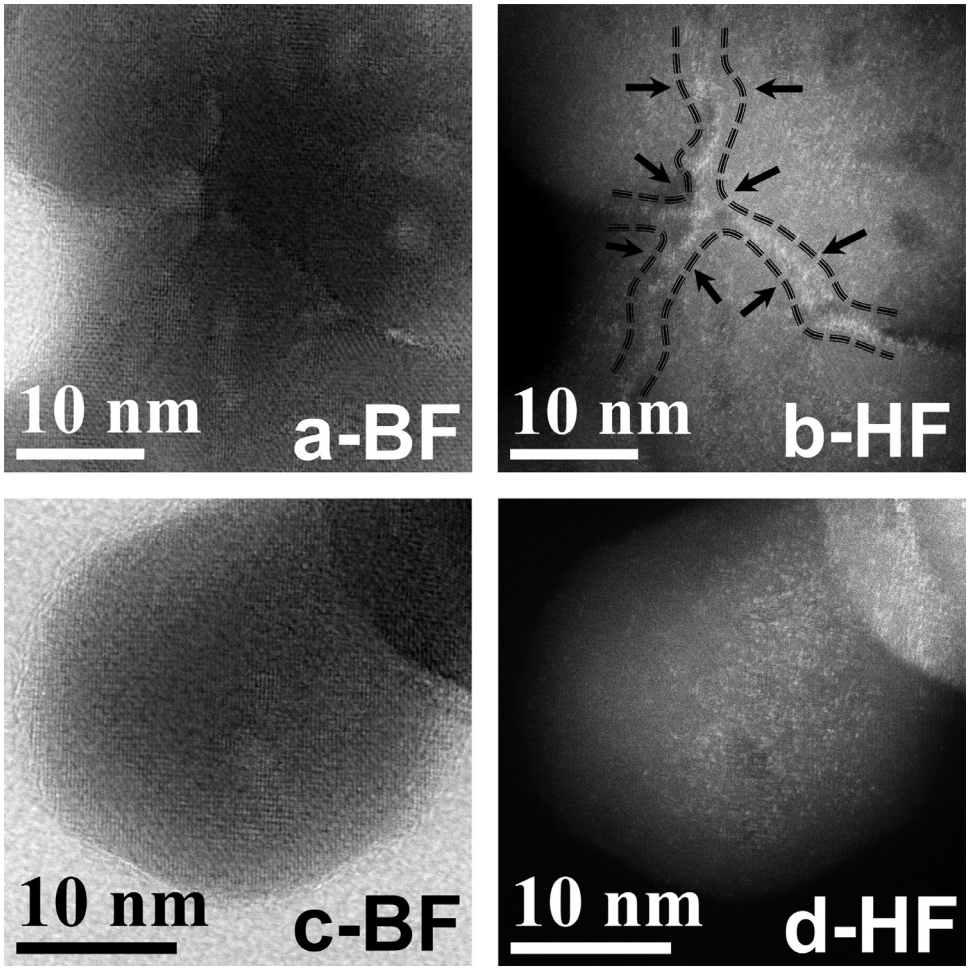

Fig. 2. Brightfield (BF) and HAADF (HF) TEM micrographs of uranium largely collected along hematite grain boundaries (a, b) and uranium evenly distributed along lattice fringes (c, d). Lines and arrows are drawn to highlight U clustering (bright from Z contrast) along hematite boundaries (b).

that found by Ilton et al., and is considerably shorter than what was reported by Marshall et al. (1.87 Å) [19,21]. The four equatorial oxygen atoms are bound slightly longer than lengths seen for oxygen atoms surrounding Fe sites (Table 1, ΔR), likely due to differences in oxidation state and the large size difference between U^{6+} (0.870 Å) and Fe^{3+} (0.785 Å) [26].

EXAFS results reveal coordination of the U-O octahedra to multiple neighboring iron sites, which serves as evidence of structural incorporation and occupation of Fe(III) sites within the hematite structure (Table 1, Figs. 3-4). Uranium is bound into distorted oxygen octahedra, comparable to local environments of U^{6+} in hematite described by Marshall et al. [21]. U-O coordination be-

Table 1
EXAFS fit results demonstrating uranium incorporation within $U_{0.033}Fe_{1.934}O_3$ (t = 24 h, 180 °C), using a k-range of 3.0 – 12.2.

U-path	CN	R_{ref} (Å) [24,25]	R_{lit} (Å)[21]	R (Å)	ΔR (Å)	σ^2 (Å^2)	ΔE_0 (eV)	$S0^2$	χ_v^2	R_{fit}
O_{Axial}	1.9	1.77(9)	1.87(2)	1.79(4)	0.01(5)	0.006(4)	−3.0 ± 1.9	1	152.7	0.0195
$O_{Equitorial-1}$	2.2	1.94(6)	2.07(2)	2.07(6)	0.13(0)	0.010(1)				
$O_{Equitorial-2}$	1.9	2.11(6)	2.23(3)	2.21(4)	0.09(8)	0.010(1)				
Fe_{Edge}	2.8	2.97(1)	3.11(2)	3.09(1)	0.12(0)	0.006(9)				
$Fe_{Corner-1}$	2.0	3.36(4)	3.45(6)	3.27(4)	−0.09(0)	0.007(2)				
$Fe_{Corner-2}$	2.0	3.70(5)	4.01(6)	3.50(4)	−0.20(1)	0.010(7)				
Fe_{Cell2}	1.0	3.98(6)	–	4.11(5)	0.12(9)	0.010(7)				
Fe_{Face}	–	2.90	2.87(3)	–	–	–				

CN – coordination number
R_{ref} – reference atomic distances in minerals containing U (liebigite) and Fe (hematite)
R_{lit} – atomic distances determined by Marshall et al. for U in hematite
R – atomic distance
ΔR – difference from reference values
σ^2 – Debye-Waller factor
ΔE_0 – energy shift from U L_{III}
$S0^2$ – amplitude factor
χ_v^2 – reduced χ square value
R_{fit} – goodness of fit.

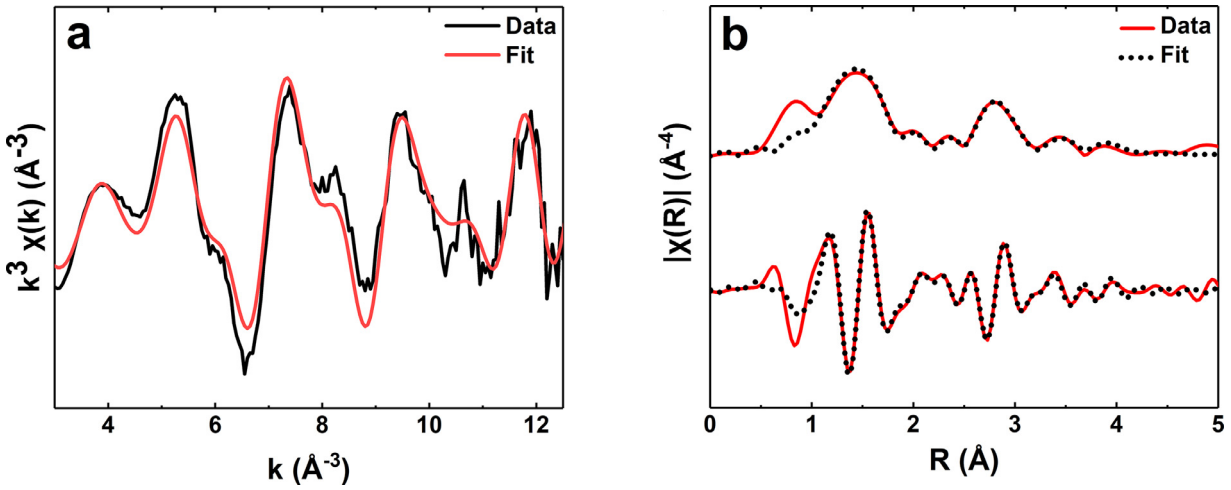

Fig. 3. Uranium L_{III}-edge EXAFS spectra (a) and Fourier transform (b) from U(VI)-incorporated hematite, $U_{0.033}Fe_{1.934}O_3$.

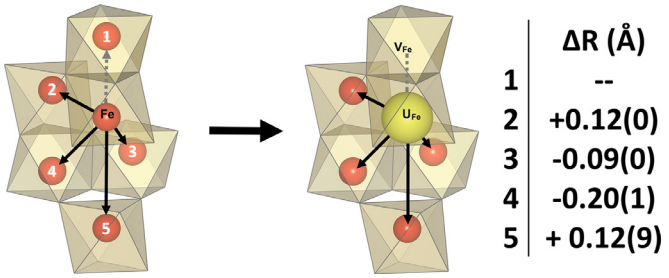

	ΔR (Å)
1	--
2	+0.12(0)
3	-0.09(0)
4	-0.20(1)
5	+ 0.12(9)

Fig. 4. Effects of U-Fe substitution on local coordination within hematite structure, as calculated from U L_{III} EXAFS. Calculated distances are compared to literature results in Table 1.

tween the studies agree, with two uranyl-like axial bonds and four hematite-like equatorial bonds. U-Fe shells are resolved up to 4.11 Å, most notably with the absence of the face-sharing (nearest neighboring; 2.90 Å) Fe shell. This finding is partially corroborated by AIMD calculations of vacancy configurations for U in hematite by McBriarty et al., where the single face-sharing vacancy results in the lowest energy structure [20]. However, this result conflicts with conclusions by them and others that charge compensation is accomplished by two opposing corner-sharing vacancies – despite being the highest calculated energy (least favorable) configuration.

Results from U L_{III} XANES suggest uranium to be retained as fully oxidized U(VI). Resonance features comparable to existing U L_{III} XANES spectra on hematite are visible around 17,187 eV and 17,220 eV (Figure A.6) [19–21]. The higher energy feature (indicative of longer U—O equatorial bonds) is present in both U(IV) and U(VI) spectra, while the visible lower energy feature (indicative of short axial $U = O$ bonds) is not present in U(IV) spectra [27].

3.3. Stoichiometry – dehydration

Quantifying the amount of hydration per unit of solid is needed to account for its contribution to calorimetric results. Drying at 80 °C for over 12 h removes weakly physisorbed water. However, the small size and corresponding high surface area result in considerable amounts of strongly chemisorbed water. These water molecules require additional energy from higher temperatures to detach from the nanoparticle surfaces. From TGA, this water content ranges between 0.025 – 0.030 mol H_2O/mol Fe_2O_3. Water-corrected enthalpy measurements ($\Delta H_{ds\text{-}H2O,\ 700\ °C}$) are reported in Table 2. DSC curves consistently reveal the onset of an endothermic event near 290 °C with no inflection in the TGA slope. This finding suggests a structural change at elevated temperatures, possibly due to aggregation of the nanoparticles while still slightly hydrated. Representative TGA and DSC traces are shown in Figure A.4.

3.4. Stoichiometry - uranium remobilization and retention pathways

Uranium concentrations within solid hematite samples were calculated from ICP-MS of acid-digested solids and are reported in Table 2. A range of 1.1 – 3.7 mol% U was incorporated in our samples, representing a 2 to 5-fold increase from 0.6 – 0.7 mol% U samples explored in previous studies [16,19–21,28] Additionally, the supernatant from five samples after hydrothermal treatment were evaluated to confirm that negligible amounts of uranium and iron remained in solution. This finding shows that all the uranium and iron had effectively been immobilized. Mass balance calculations were then used with ICP-MS data to determine the amount of uranium that had been weakly adsorbed to precipitate surfaces, coprecipitated into acid-unstable (< pH 2.5) solids, and strongly incorporated within hematite particles (final product).

The relative amounts of uranium partitioned to each pathway are shown as a function of initial uranyl concentration in Fig. 5. ICP-MS results reveal that uranium loading within hematite increased at higher uranyl concentrations. However, a smaller proportion of total U(VI) becomes incorporated, with the remainder favorably adsorbing or coprecipitating outside of the hematite particles. With increasing uranyl concentrations, the immobilization pathways by which hematite retains uranium shifted dramatically. While all aqueous uranium was captured from each tested synthesis condition, the most favorable route at lower uranyl concentrations was incorporation. Uranium incorporation became progressively more challenging to achieve with higher uranium concentrations in solution.

3.5. Thermodynamic measurements

The stoichiometry of chemisorbed water for each sample was measured by dehydration during TGA. To determine the formation enthalpies of the oxides themselves, hydration contributions needed to be removed. Fine-grained hematite has two stages and corresponding enthalpies of chemisorption to account for. Approximately 71% of total water is weakly chemisorbed (−25.5 ± 4.4 kJ/mol H_2O), with the remaining 29% being more strongly chemisorbed (−67.1 ± 4.9 kJ/ mol H_2O) relative to weak adsorption of liquid bulk water [29]. Contributions from bulk water *de*sorption is defined as 69.0 kJ/mol H_2O, which is the enthalpy

Table 2
Measured and calculated thermodynamic properties for $U_xFe_{2-2x}O_3$. $\Delta H°_{f,ox}$ is calculated as standard formation enthalpy of the mixed oxide relative to the weighted values for α-Fe_2O_3 and γ-UO_3.

x (mol U)	n (mol H_2O)	$[U_0]_{(mM)}$	t_{rxn} (hr)	$\Delta H_{ds,\ 700°C}$ (kJ/mol)	$\Delta H_{ds\text{-}H2O,\ 700°C}$ (kJ/mol)	$\Delta H°_{f,\ el}$ (kJ/mol)	$\Delta H°_{f,\ ox}$ (kJ/mol)
0.000(0)	0.000	0.00	24	91.06 ± 0.88	91.06 ± 0.88	−821.63 ± 2.39	4.57 ± 1.83
0.013(0)	0.417	0.28	24	99.47 ± 1.28	55.10 ± 1.92	−791.93 ± 2.30	39.41 ± 1.98
0.015(3)	0.264	3.15	24	88.13 ± 1.08	60.00 ± 1.41	−797.97 ± 1.53	34.31 ± 1.50
0.033(0)	0.488	5.25	24	90.86 ± 0.73	38.87 ± 1.83	−785.41 ± 2.16	53.92 ± 1.89
0.011(5)	0.222	0.28	72	87.66 ± 1.32	63.96 ± 1.52	−800.07 ± 1.69	30.68 ± 1.60
0.014(8)	0.228	0.46	72	89.11 ± 0.75	64.87 ± 1.08	−802.61 ± 1.09	29.48 ± 1.19
0.024(1)	0.199	3.15	72	68.13 ± 1.19	46.95 ± 1.37	−789.19 ± 1.47	46.60 ± 1.46
0.037(0)	0.219	5.25	72	38.87 ± 2.69	15.55 ± 2.79	−764.04 ± 3.74	76.88 ± 2.83

n – excess water bound by chemisorption and physisorption.
$[U_0]$ – initial uranyl concentration.
t_{txn} – hydrothermal treatment time.
$\Delta H_{ds,\ 700\ °C}$ – measured enthalpy of drop solution.
$\Delta H_{ds\text{-}H2O,\ 700\ °C}$ – water-corrected enthalpy of drop solution.
$\Delta H°_{f,\ el}$ – standard formation enthalpy relative to constituent elements.
$\Delta H°_{f,\ ox}$ – standard formation enthalpy relative to binary oxides.

of heating liquid water at ambient temperature to form and release water vapor in the oxide melt solution calorimeter at 700 °C [30]. The total dehydration energetics are subtracted from measured oxide melt solution values (ΔH_{ds}) at 700 °C. Water-corrected enthalpies are reported as $\Delta H_{ds\text{-}H2O,\ 700}$ °C and are used for subsequent thermodynamic calculations. Enthalpies for the uranium-free sample were calculated using published data, where water content was already accounted for [31,32]. A summary of uranium concentrations and corresponding thermodynamic values is provided in Table 2. Enthalpic trends for different reaction times are shown as functions of uranium concentrations in Fig. 6. A lower maximum U concentration and smaller thermodynamic penalty were observed for samples with shorter treatment times. The thermochemical cycle and reactions used to calculate these values are outlined in Table 3.

Decreased stability from high surface areas contributed to measured calorimetric values of nanoparticles. Nanoscale α-Fe_2O_3 has been reported to have a surface energy of 1.9 ± 0.3 J/m^2 [31]. BET surface areas from analogous uranium-free powders averaged 2403 ± 13 m^2/mol and are assumed to be comparable to those for uranium-loaded samples. Our reference point for measured calorimetric values was a uranium-free hematite of comparable surface area. In doing so, surface energetics of nanoparticles are removed from enthalpy calculations relative to binary oxides [32].

Formation enthalpies with any amount of uranium indicate metastability relative to separate binary oxides (α-Fe_2O_3 and UO_x) (Table 2, $\Delta H°_{f,\ ox}$). With increasing uranium concentration, the energetic stability of the composite oxide decreases relative those of its binary oxide constituents. Relative to binary oxides, structural incorporation increases (makes less exothermic) the formation enthalpy of the mixed oxide.

4. Discussion

4.1. Local u coordination

Including the face-sharing shell significantly worsened the EXAFS fit in our study. Meanwhile, F-tests showed high confidence of its absence, as opposed to all other Fe shells being present (including corner-sharing sites) with high confidence (Table A.1, A.2) [35]. The Fe site 2.90 Å from the central atom is consistently absent and we propose this serves as the charge compensation mechanism for U(VI) occupying an Fe(III) site. This site was closest and most subject to strain from the adjacent U atom. Presumably, forming this vacant site alleviated the strain and distortion induced by U-Fe substitution. The innermost and outermost resolved U-Fe shells expanded relative to reference hematite inter atomic distances, whereas the intermediate length sites contracted.

Acquired EXAFS data partially agree with existing literature on uranium-incorporated hematite, in that uranium substitutes for Fe within the hematite structure. Differences in interpretations primarily revolve around U-Fe shells and vacancy formation. Earlier work by Marshall et al. found the face-sharing site to be present with a shorter U-Fe distance (2.87 Å) than its normal Fe-Fe length (2.90 Å) [21]. Other U-Fe shells appear in agreement, although the

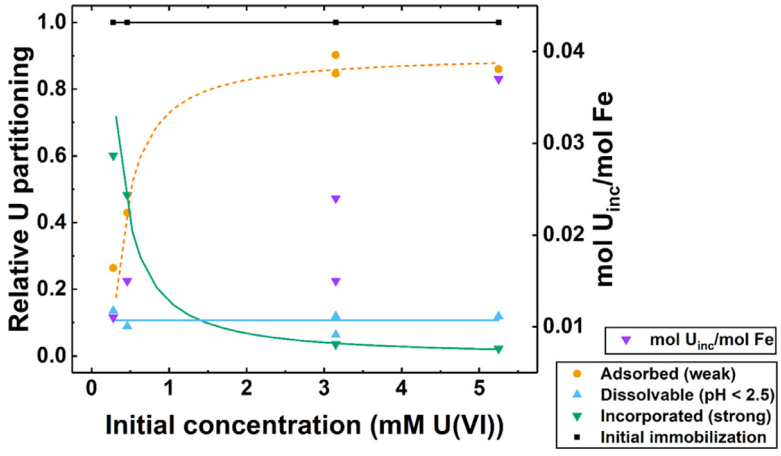

Fig. 5. Effect of U_0 on uranium partitioning to immobilization pathways, based on ICP-MS calculations and shown as fractions of total uranium in system.

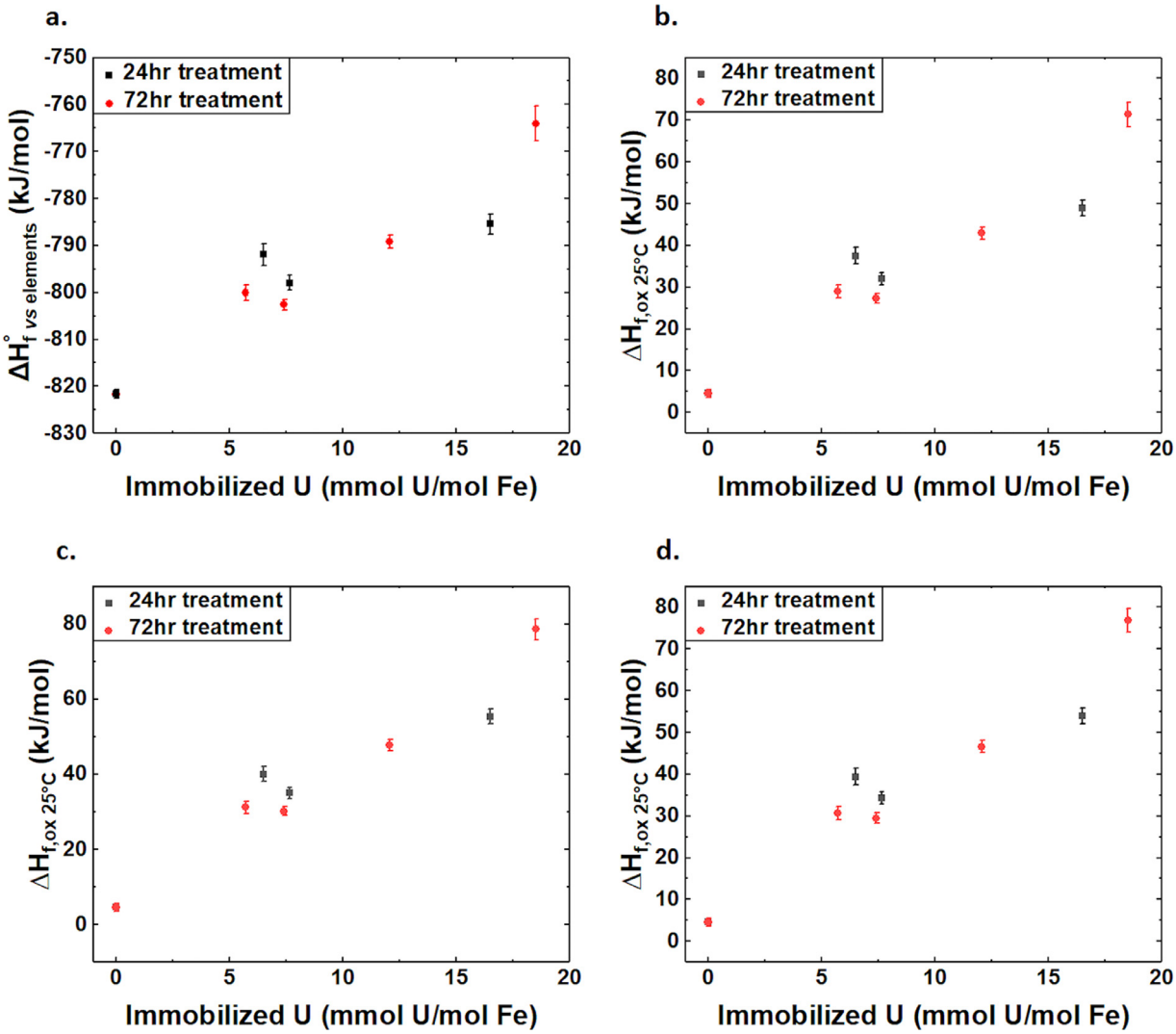

Fig. 6. Formation enthalpy of uranium-incorporated α-Fe_2O_3 in relation to constituent elements (U, F, O) (a), binary oxides (UO_2, α-Fe_2O_3) (b), binary oxides (U_3O_8, α-Fe_2O_3) (c), binary oxides (γ-UO_3, α-Fe_2O_3) (d).

outermost shell had not previously been resolved. Meanwhile, *ab initio* guided EXAFS work by McBriarty et al. determined iron vacancy formation at opposing corners (2C) from the central uranium site [20]. This geometry fit best with their EXAFS data, despite being the highest calculated energy configuration. In contrast, our result of a single face-sharing vacancy (F) agrees with their lowest energy configuration. They report the 2C configuration to best fit their EXAFS data, although comparisons were shown for 2C+*F* rather than F alone. Later studies by Ilton et al. found that vacancies at *trans*-corner and face-sharing sites may form [28]. It is possible that these conflicting conclusions are all valid. The specific coordination environment of U within hematite may be highly sensitive to differences in synthesis and incorporation processes.

Observed differences in local U coordination may result from a variety of experimental conditions. Our study used single-phase samples, which prevented convoluting our findings with those of goethite. Formation of the face-sharing vacancy configuration may be unique to hematite formation at elevated temperatures (e.g., 180 °C), and it is unclear if the same may be observed at the lower ambient temperatures seen in other studies. Our results indicate that uranium enters and is stabilized within the hematite structure, all while maintaining the uranyl-like coordination of the axial oxygen bonds. Considering the similarities in EXAFS spectra among existing literature, it may be presumed that our hydrothermal synthesis conditions do not severely alter the coordination environments from those resulting from ageing under ambient conditions.

4.2. Uranium partitioning

Uranium may be well retained through two routes within hematite nanoparticles. As evidenced by TEM, uranium atoms may cluster along the boundaries of hematite aggregates and along hematite lattice fringes (Fig. 2b). In addition, EXAFS interpretations confirm uranium can occupy iron sites throughout the host structure. Uranium immobilization pathways under hydrothermal conditions may vary depending on treatment duration and initial uranyl concentrations. Possibly more important in dictating concentration of well-incorporated U is reaction time. Samples subjected to elevated temperatures for 24 h tended to result in lower U loadings (and lower formation enthalpies) than those held for 72 h (Table 2, Fig. 6). These results may highlight the practical differences in incorporated uranium collection primarily along grain boundaries compared to homogeneous lattice substitution.

We hypothesize the 24-h reaction time to favor formation of α-Fe_2O_3 with UO_x clustering along its grain boundaries. Extending reaction times to 72 h is expected to result in increased U migration kinetics and greater U-Fe substitution. The differences from treatment times in this study are speculated to result from kinetic

Table 3
Thermochemical reactions used to calculate standard formation enthalpies.

	Reactions - Enthalpy of formation of $U_xFe_{2-2x}O_3$ from elements and from oxides at 25 °C	Enthalpy, ΔH (kJ/mol)	References
1	$U_xFe_{2-2x}O_{3\,(s,\ 25°C)} \rightarrow (1-x)Fe_2O_{3\,(sln,\ 700°C)} + xUO_{3\,(sln,\ 700°C)}$ for $0 < x < 0.037$	$\Delta H_1 = \Delta H_{ds}$	
2	$\alpha - Fe_2O_{3\,(s,\ 25°C)} \rightarrow Fe_2O_{3\,(sln,\ 700°C)}$	$\Delta H_2 = 91.06 \pm 0.88^*$ (nano)	[31,32]
3a	$\gamma - UO_{3\,(s,\ 25°C)} \rightarrow UO_{3\,(sln,\ 700°C)}$	$\Delta H_{3a} = 9.49 \pm 1.53$	[33]
3b	$\frac{1}{3}U_3O_{8\,(s,\ 25°C)} + \frac{1}{6}O_{2\,(g,\ 25°C)} \rightarrow UO_{3\,(sln,\ 700°C)}$	$\Delta H_{3b} = 54.0 \pm 6.4$	[33]
3c	$UO_{2\,(s,\ 25°C)} + \frac{1}{2}O_{2\,(g,\ 25°C)} \rightarrow UO_{3\,(sln,\ 700°C)}$	$\Delta H_{3c} = -140.4 \pm 2.67$	[33]
4	$2Fe_{(s,\ 25°C)} + \frac{3}{2}O_{2\,(g,\ 25°C)} \rightarrow \alpha - Fe_2O_{3\,(s,\ 25°C)}$	$\Delta H_4 = -826.2 \pm 1.3$	[34]
5	$U_{(s,\ 25°C)} + \frac{3}{2}O_{2\,(g,\ 25°C)} \rightarrow \gamma - UO_{3\,(s,\ 25°C)}$	$\Delta H_5 = -1223.8 \pm 0.8$	[34]
6a	$(1-x)Fe_2O_{3\,(s,\ 25°C)} + xUO_{3\,(s,\ 25°C)} \rightarrow U_xFe_{2-2x}O_{3\,(s,\ 25°C)}$	$\Delta H_{6a} = \Delta H_{f,\,ox1}$	
6b	$(1-x)Fe_2O_{3\,(s,\ 25°C)} + \frac{x}{3}U_3O_{8\,(s,\ 25°C)} + \frac{x}{6}O_{2\,(g,\ 25°C)} \rightarrow U_xFe_{2-2x}O_{3\,(s,\ 25°C)}$	$\Delta H_{6b} = \Delta H_{f,\,ox2}$	
6c	$(1-x)Fe_2O_{3\,(s,\ 25°C)} + xUO_{2\,(s,\ 25°C)} + \frac{x}{2}O_{2\,(g,\ 25°C)} \rightarrow U_xFe_{2-2x}O_{3\,(s,\ 25°C)}$	$\Delta H_{6c} = \Delta H_{f,\,ox3}$	
7	$xU_{(s,\ 25°C)} + (2-2x)Fe_{(s,\ 25°C)} + \frac{3+y}{2}O_{2\,(g,\ 25°C)} \rightarrow U_xFe_{2-2x}O_{3\,(s,\ 25°C)}$	$\Delta H_7 = \Delta H_{f.,\,el}$	

*Corrected from bulk to nanoscale (2403 m^2/mol) with 4.57 kJ/mol surface energy.
$\Delta H_{f,\ ox1} = -\Delta H_1 + (1-x)\ \Delta H_2 + x\ \Delta H_{3a}$.
$\Delta H_{f,\ ox2} = -\Delta H_1 + (1-x)\ \Delta H_2 + x\ \Delta H_{3b}$.
$\Delta H_{f,\ ox3} = -\Delta H_1 + (1-x)\ \Delta H_2 + x\ \Delta H_{3c}$.
$\Delta H_{f,\ el} = -\Delta H_1 + (1-x)\ \Delta H_2 + x\ \Delta H_3 + (1-x)\ \Delta H_4 + x\ \Delta H_5$.
for $0 < x < 0.037$.

limitations, where even 72 h may not have been long enough to reach equilibrium in the vessel at 180 °C. The recent study by Ilton et al. [28] employed a combination of time-resolved HAADF-STEM and AIMD to demonstrate the dynamics of uranium atoms within hematite nanoparticles. They showed U atoms to hop or diffuse across vacancies in the hematite when energized by an electron beam or when simulated with increasing temperatures and simulation times. Their findings may be applicable to this study, where elevated temperatures would enable U migration during and after hematite crystallization, while longer periods at elevated temperatures provide more opportunities and greater distances for U to travel. Extended hydrothermal treatment facilitates uranium mobilization throughout the iron oxide lattice. The kinetics of uranium immobilization by this technique may be elucidated in the future by exploring lengthier time periods and a wider range of hydrothermal conditions. Such findings may help exploit and optimize iron oxide nanoparticles for capture and storage of aqueous uranium from solution.

4.3. Energetics of uranium incorporation

We postulate that thermodynamic trends from this study are applicable to similar cases in which uranium is well-retained within hematite nanoparticles. Less directly applicable are specific thermodynamic values at given uranium concentrations. For studies where higher-energy vacancy configurations are found (e.g., 2C), it is possible that the overall formation enthalpy is consequently shifted upwards (less stable/more metastable).

At higher concentrations of well-retained uranium, the energetic stability of 24-h samples is greater (lower $\Delta H°_f$) than that of 72-h samples (higher $\Delta H°_f$). In both cases, entropic contributions probably facilitate this incorporation behavior. However, the extent to which incorporation occurs is kinetically limited, as suggested by the 5.25 mM U(VI) starting solution retaining more U in the final solid after 72 h (3.7 mol% U) rather than 24 h (3.3 mol% U). The enthalpic differences resulting from varying hydrothermal treatment times also suggest that equilibrium had not been reached in these metastable oxides. As a result, entropy terms could not be calculated, and the roles of incorporation kinetics and entropic contributions in the studied samples remain unclear. It may be relevant to consider that extended hydrothermal treatment times typically allow nanoparticles to fully crystallize, aggregate, grow, and ultimately stabilize [22]. If contaminated with aqueous uranyl species under such conditions, adsorbed uranium atoms are provided the opportunity to favorably diffuse into the iron oxide lattice. We therefore hypothesize that accelerated diffusion kinetics and expansion of the host lattice under elevated synthesis temperatures enable gradual uranium migration into Fe sites.

Thermodynamic results reveal an interplay between maximizing uranium concentration within hematite and maximizing energetic stability of the contained uranium. Such interplay is heavily dependent on synthesis conditions, which determine grain boundaries/solid solutions with uranium oxides versus U_{Fe} substitution throughout nanoparticle lattices. Shorter treatment times appear to favor higher relative concentrations along interfaces. The structurally confined uranium in this scenario may come from limited amounts of uranium along ferrihydrite surfaces being trapped in place during the aggregation and transformation of ferrihydrite to hematite. Meanwhile, extended hydrothermal treatment times appear to facilitate higher incorporation. Uranium aggregates along grain boundaries are provided more time to diffuse within the iron oxide lattice and then remain trapped after cooling to ambient temperature. Reported formation enthalpies represent the stability of hematite with strongly bound uranium within its structure. However, quantitative distinctions in stability between pure lattice incorporation and pure grain boundary confinement cannot be made. Our findings suggest a lower energy cost and higher stability with grain boundary confinement under circumneutral environments, at the cost of increased uranium remobilization potential under acidic conditions.

5. Conclusions

Results from this project provide data essential for understanding the fate of uranium in geological disposal sites over extended timescales, and the transport of uranium in the environment. Identifying the stability of structural incorporation suggests the feasibility of iron oxides for inhibiting the mobility of aqueous uranium(VI). Environmentally abundant iron-bearing minerals, and corrosion products from steel containment barriers for radioactive waste, may play a crucial role in inhibiting uranium species mobility upon eventual leaching into the environment. These insights, including new thermodynamic data, will help guide the modeling and improvement of safe and scalable radioactive waste disposal practices and water remediation applications, which ultimately improve water safety for humans and surrounding ecosystems.

Declaration of Competing Interest

The authors declare that they have no known competing financial interests or personal relationships that could have appeared to influence the work reported in this paper.

CRediT authorship contribution statement

Andy Lam: Conceptualization, Data curation, Formal analysis, Investigation, Methodology, Project administration, Validation, Visualization, Writing – original draft, Writing – review & editing. **Forrest Hyler:** Formal analysis, Visualization, Writing – review & editing. **Olwen Stagg:** Formal analysis, Validation, Writing – original draft. **Katherine Morris:** Conceptualization, Methodology, Resources, Supervision, Funding acquisition. **Samuel Shaw:** Conceptualization, Methodology, Resources, Supervision, Funding acquisition, Writing – original draft, Writing – review & editing. **Jesús M. Velázquez:** Conceptualization, Methodology, Resources, Supervision, Funding acquisition, Writing – original draft, Writing – review & editing. **Alexandra Navrotsky:** Conceptualization, Methodology, Validation, Resources, Supervision, Funding acquisition, Writing – original draft, Writing – review & editing.

Acknowledgements

This work was supported by the U.S. Department of Energy, Office of Basic Energy Sciences, grant DE-FG02-97ER14749 (Thermodynamics of Minerals Stable near Earth's Surface). Support was also provided by the Nuclear Regulatory Commission (31310019M0009) through the Advancing Scientific Careers to Enhance Nuclear Technologies (ASCENT) program. We thank the University of California, Davis for start-up funding, as well as the Research Corporation for Science Advancement (RCSA 26780) through the Cottrell Scholar program. We also acknowledge funding support from the NSF through the Faculty Early Career Development Program (DMR-2044403). Diamond Light Source provided beam-time (SP17243), and the authors thank Steve Parry for his beamline assistance.

Supplementary materials

Supplementary material associated with this article can be found, in the online version, at doi:10.1016/j.jnucmat.2021.153172.

References

[1] A. Chen, C. Shang, J. Shao, J. Zhang, H. Huang, The application of iron-based technologies in uranium remediation: a review, Sci. Total Environ. 575 (2017) 1291–1306, doi:10.1016/j.scitotenv.2016.09.211.
[2] P. Kurttio, A. Auvinen, L. Salonen, H. Saha, J. Pekkanen, I. Mäkeläinen, S.B. Väisänen, I.M. Penttilä, H. Komulainen, Renal effects of uranium in drinking water, Environ. Health Perspect. 110 (2002) 337–342, doi:10.1289/ehp.02110337.
[3] K.G. Orloff, K. Mistry, P. Charp, S. Metcalf, R. Marino, T. Shelly, E. Melaro, A.M. Donohoe, R.L. Jones, Human exposure to uranium in groundwater, Environ. Res. 94 (2004) 319–326, doi:10.1016/S0013-9351(03)00115-4.
[4] R.A. Peterson, E.C. Buck, J. Chun, R.C. Daniel, D.L. Herting, E.S. Ilton, G.J. Lumetta, S.B. Clark, Review of the scientific understanding of radioactive waste at the U.S. DOE Hanford site, Environ. Sci. Technol. 52 (2018) 381–396, doi:10.1021/acs.est.7b04077.
[5] Final Review of the Study on Supplemental Treatment Approaches of Low-Activity Waste At the Hanford Nuclear Reservation, 2020, doi:10.17226/25710.
[6] A. Goel, J.S. McCloy, R. Pokorny, A.A. Kruger, Challenges with vitrification of Hanford High-Level Waste (HLW) to borosilicate glass – an overview, J. Non-Crystalline Solids X. 4 (2019) 100033, doi:10.1016/j.nocx.2019.100033.
[7] D.J. Wronkiewicz, Effects of Radionuclide Decay On Waste Glass Behaviour - A Critical Review, ANL-93/45, Argonne National Laboratory, Argonne, IL, 1993.
[8] W.G. Burns, A.E. Hughes, J.A.C. Marples, R.S. Nelson, A.M. Stoneham, Effects of radiation on the leach rates of vitrified radioactive waste, J. Nucl. Mater. 107 (1982) 245–270, doi:10.1016/0022-3115(82)90424-X.
[9] R.M. Cornell, U. Schwertmann, The iron oxides, in: Iron Oxides Laboratary, Wiley-VCH Verlag GmbH, Weinheim, Germany, 2003, pp. 5–18, doi:10.1002/9783527613229.ch01.
[10] H. Zeng, A. Singh, S. Basak, K.-.U. Ulrich, M. Sahu, P. Biswas, J.G. Catalano, D.E. Giammar, Nanoscale size effects on uranium(VI) adsorption to hematite, Environ. Sci. Technol. 43 (2009) 1373–1378, doi:10.1021/es802334e.
[11] X. Shuibo, Z. Chun, Z. Xinghuo, Y. Jing, Z. Xiaojian, W. Jingsong, Removal of uranium (VI) from aqueous solution by adsorption of hematite, J. Environ. Radioact. 100 (2009) 162–166, doi:10.1016/j.jenvrad.2008.09.008.
[12] C.H. Ho, D.C. Doern, The sorption of uranyl species on a hematite sol, Can. J. Chem. 63 (1985) 1100–1104, doi:10.1139/v85-186.
[13] T. Phuengprasop, J. Sittiwong, F. Unob, Removal of heavy metal ions by iron oxide coated sewage sludge, J. Hazard. Mater. 186 (2011) 502–507, doi:10.1016/j.jhazmat.2010.11.065.
[14] T.D. Waite, J.A. Davis, T.E. Payne, G.A. Waychunas, N. Xu, Uranium(VI) adsorption to ferrihydrite: application of a surface complexation model, Geochim. Cosmochim. Acta. 58 (1994) 5465–5478, doi:10.1016/0016-7037(94)90243-7.
[15] T. Ohnuki, H. Isobe, N. Yanase, T. Nagano, Y. Sakamoto, K. Sekine, Change in sorption characteristics of uranium during crystallization of amorphous iron minerals, J. Nucl. Sci. Technol. 34 (1997) 1153–1158, doi:10.1080/18811248.1997.9733805.
[16] M.C. Duff, J.U. Coughlin, D.B. Hunter, Uranium co-precipitation with iron oxide minerals, Geochim. Cosmochim. Acta. 66 (2002) 3533–3547, doi:10.1016/S0016-7037(02)00953-5.
[17] K.S. Smith, Metal sorption on mineral surfaces, in: Environ. Geochemistry Miner. Depos., Society of Economic Geologists, 1997, pp. 161–182, doi:10.5382/Rev.06.07.
[18] T.A. Marshall, K. Morris, G.T.W.W. Law, J.F.W. Mosselmans, P. Bots, H. Roberts, S. Shaw, Uranium fate during crystallization of magnetite from ferrihydrite in conditions relevant to the disposal of radioactive waste, Mineral. Mag. 79 (2015) 1265–1274, doi:10.1180/minmag.2015.079.6.02.
[19] E.S. Ilton, J.S.L. Pacheco, J.R. Bargar, Z. Shi, J. Liu, L. Kovarik, M.H. Engelhard, A.R. Felmy, Reduction of U(VI) incorporated in the structure of hematite, Environ. Sci. Technol. 46 (2012) 9428–9436, doi:10.1021/es3015502.
[20] M.E. McBriarty, S. Kerisit, E.J. Bylaska, S. Shaw, K. Morris, E.S. Ilton, Iron vacancies accommodate uranyl incorporation into hematite, Environ. Sci. Technol. 52 (2018) 6282–6290, doi:10.1021/acs.est.8b00297.
[21] T.A. Marshall, K. Morris, G.T.W. Law, F.R. Livens, J.F.W. Mosselmans, P. Bots, S. Shaw, Incorporation of uranium into hematite during crystallization from ferrihydrite, Environ. Sci. Technol. 48 (2014) 3724–3731, doi:10.1021/es500212a.
[22] Y. Hao, A.S. Teja, Continuous hydrothermal crystallization of α–Fe_2O_3 and Co_3O_4 nanoparticles, J. Mater. Res. 18 (2003) 415–422, doi:10.1557/JMR.2003.0053.
[23] U.T. Lam, R. Mammucari, K. Suzuki, N.R. Foster, Processing of iron oxide nanoparticles by supercritical fluids, Ind. Eng. Chem. Res. 47 (2008) 599–614. 10.1021/ie070494.
[24] E.N. Maslen, V.A. Streltsov, N.R. Streltsova, N. Ishizawa, Synchrotron X-ray study of the electron density in α-Fe_2O_3, Acta Crystallogr. Sect. B 50 (1994) 435–441, doi:10.1107/S0108768194002284.
[25] K. Mereiter, The crystal structure of Liebigite, Ca2UO2(CO3)3•~11H2O, TMPM tschermaks mineral. Und Petrogr. Mitteilungen. 30 (1982) 277–288. 10.1007/BF01087173.
[26] R.D. Shannon, Revised effective ionic radii and systematic studies of interatomic distances in halides and chalcogenides, Acta Crystallogr. Sect. A. 32 (1976) 751–767, doi:10.1107/S0567739476001551.
[27] F. Farges, C.W. Ponader, G. Calas, G.E. Brown, Structural environments of incompatible elements in silicate glass/melt systems: II. UIV, UV, and UVI, Geochim. Cosmochim. Acta. 56 (1992) 4205–4220. 10.1016/0016-7037(92)90261-G.
[28] E.S. Ilton, L. Kovarik, E. Nakouzi, S.T. Mergelsberg, M.E. McBriarty, E.J. Bylaska, Using atom dynamics to map the defect structure around an impurity in nanohematite, J. Phys. Chem. Lett. 11 (2020) 10396–10400, doi:10.1021/acs.jpclett.0c02798.
[29] L. Mazeina, A. Navrotsky, Enthalpy of water adsorption and surface enthalpy of goethite (α-FeOOH) and hematite (α-Fe_2O_3), Chem. Mater. 19 (2007) 825–833, doi:10.1021/cm0623817.
[30] M.W. Chase, NIST-JANAF Thermochemical Tables, 4th Ed. J. Phys. Chem. Ref. Data. 1998, monograph 9(Part I and Part II), J. Phys. Chem. Ref. Data. Monograph (1998) Part I&II.
[31] A. Navrotsky, C. Ma, K. Lilova, N. Birkner, Nanophase transition metal oxides show large thermodynamically driven shifts in oxidation-reduction equilibria, Science 330 (80) (2010) 199–201, doi:10.1126/science.1195875.
[32] J. Majzlan, A. Navrotsky, B.J. Evans, Thermodynamics and crystal chemistry of the hematite-corundum solid solution and the $FeAlO_3$ phase, Phys. Chem. Miner. 29 (2002) 515–526, doi:10.1007/s00269-002-0261-7.
[33] X. Guo, S. Szenknect, A. Mesbah, S. Labs, N. Clavier, C. Poinssot, S.V. Ushakov, H. Curtius, D. Bosbach, R.C. Ewing, P.C. Burns, N. Dacheux, A. Navrotsky, in: Thermodynamics of formation of coffinite, $USiO_4$, 112, 2015, pp. 6551–6555, doi:10.1073/pnas.1507441112.
[34] R.A. Robie, B.S. Hemingway, Thermodynamic Properties of Minerals and Related Substances at 298.15K and 1Bar (105 Pa) and at Higher Temperatures (1995).
[35] L. Downward, C.H. Booth, W.W. Lukens, F. Bridges, A variation of the F-test for determining statistical relevance of particular parameters in EXAFS fits, in: AIP Conf. Proc., 2007. 10.1063/1.2644450.